The shape and size distribution of H II regions near the percolation transition

Article (Published Version)

Monthly Notices of the ROYAL ASTRONOMICAL SOCIETY

MNRAS **477,** 1984–1992 (2018) doi:10.1093/mnras/sty714
Advance Access publication 2018 March 19

The shape and size distribution of H II regions near the percolation transition

Satadru Bag,[1]★ Rajesh Mondal,[2,3] Prakash Sarkar,[4] Somnath Bharadwaj[3] and Varun Sahni[1]

[1]*Inter-University Centre for Astronomy and Astrophysics, Pune 411007, India*
[2]*Department of Physics and Astronomy, Astronomy Centre, University of Sussex, Brighton BN19QH, UK*
[3]*Department of Physics and Centre for Theoretical Studies, Indian Institute of Technology Kharagpur, Kharagpur 721302, India*
[4]*National Institute of Technology, Jamshedpur 831014, India*

Accepted 2018 March 15. Received 2018 March 11; in original form 2018 January 29

ABSTRACT

Using Shapefinders, which are ratios of Minkowski functionals, we study the morphology of neutral hydrogen (H I) density fields, simulated using seminumerical technique (inside-out), at various stages of reionization. Accompanying the Shapefinders, we also employ the 'largest cluster statistic' (LCS), originally proposed in Klypin & Shandarin, to study the percolation in both neutral and ionized hydrogen. We find that the largest ionized region is percolating below the neutral fraction $x_{\rm H\,I} \lesssim 0.728$ (or equivalently $z \lesssim 9$). The study of Shapefinders reveals that the largest ionized region starts to become highly filamentary with non-trivial topology near the percolation transition. During the percolation transition, the first two Shapefinders – 'thickness' (T) and 'breadth' (B) – of the largest ionized region do not vary much, while the third Shapefinder – 'length' (L) – abruptly increases. Consequently, the largest ionized region tends to be highly filamentary and topologically quite complex. The product of the first two Shapefinders, $T \times B$, provides a measure of the 'cross-section' of a filament-like ionized region. We find that, near percolation, the value of $T \times B$ for the largest ionized region remains stable at $\sim$7 Mpc^2 (in comoving scale) while its length increases with time. Interestingly, all large ionized regions have similar cross-sections. However, their length shows a power-law dependence on their volume, $L \propto V^{0.72}$, at the onset of percolation.

Key words: intergalactic medium – dark ages, reionization, first stars – large-scale structure of Universe – cosmology: theory.

1 INTRODUCTION

It is widely believed that, following the cosmological recombination of hydrogen at $z \simeq 1089$, the universe reionized at the much lower redshift of $z \sim 10$ (Planck Collaboration XVI 2014). Our current knowledge about this epoch of reionization (EoR) is guided so far by three main observations. Measurements of the Thomson scattering optical depth of cosmic microwave background (CMB) photons from free electrons (Komatsu et al. 2011; Planck Collaboration XIII 2016a; Planck Collaboration XLVI 2016b), observations of the Lyman-α absorption spectra of the high-redshift quasars (Becker et al. 2001; Fan et al. 2003; Goto et al. 2011; Becker et al. 2015) and the luminosity function and clustering properties of Lyman-α emitters (Ouchi et al. 2010; Trenti et al. 2010; Ota et al. 2017; Zheng et al. 2017). These observations, when taken together, suggest that the EoR probably extended over a wide redshift range $6 \lesssim z \lesssim 15$ (Mitra, Choudhury & Ferrara 2015; Robertson et al. 2015). Although the precise physical mechanism responsible for cosmological reionization is not known, it is widely believed that early sources of energetic photons contributing to reionization may have come from: an early generation of stars (Population III objects), galaxies, and quasars (Barkana & Loeb 2001, more exotic sources such as decaying dark matter have also been explored).

Observation of the redshifted 21-cm signal from neutral hydrogen (H I) provides an excellent means of studying the EoR and the preceding 'dark ages'. Considerable efforts are presently underway to detect the EoR 21-cm signal using ongoing and upcoming radio interferometric experiments e.g. GMRT (Paciga et al. 2013), LOFAR (van Haarlem et al. 2013; Yatawatta et al. 2013), MWA (Bowman et al. 2013; Dillon et al. 2014), PAPER (Parsons et al. 2014; Ali et al. 2015; Jacobs et al. 2015), SKA (Mellema et al. 2013; Koopmans et al. 2015), HERA (Furlanetto et al. 2009; DeBoer et al. 2017). The importance of a precise determination of the EoR, and the associated geometry and dynamics of neutral (H I) and ionized (H II) hydrogen regions, cannot be overstated. Such an

★ E-mail: satadru@iucaa.in

advance would open a new window into the physics of the early universe, shedding light on important issues including the physics of structure formation, the nature of feedback from the first collapsed objects, the nature of dark matter and perhaps even dark energy.

To explore this vibrant reionization landscape, we borrow tools originally developed for the understanding and analysis of the cosmic web, which is similarly rich in geometrical properties. For this purpose, we use percolation analysis[1] (Shandarin 1983; Klypin & Shandarin 1993) in conjunction with the Shapefinders, which are introduced in Sahni, Sathyaprakash & Shandarin (1998) as ratios of Minkowski functionals, to assess the morphology of reionized H II regions at different redshifts. These geometrical tools therefore play a role that is complementary to that of traditional N-point correlation functions. Our main method of analysis shall be the computationally advanced version of the SURFGEN algorithm (Sheth et al. 2003) that, in the context of structure formation, provides a means of determining the geometrical and topological properties of isodensity contours delineating superclusters and voids within the cosmic web (Sheth 2004; Shandarin, Sheth & Sahni 2004; Sheth & Sahni 2005). In this paper, we refine and adapt this algorithm to determine the shapes and sizes of H II regions at different redshifts. The physics underlying cosmological reionization is expected to be reflected in the geometry and morphology of H I and H II regions. For instance, the topology and morphology of reionization would be different if it were driven by a few quasars instead of numerous galaxies.

In recent times, many efforts have been made to understand reionization from geometrical points of view including granulometry (Kakiichi et al. 2017), percolation analyses (Iliev et al. 2006, 2014; Furlanetto & Oh 2016), and the Minkowski functionals (Friedrich et al. 2011; Kapahtia et al. 2017; Yoshiura et al. 2017). Our work, presented in this first of a series of papers, would be unique and interesting for two following reasons. First, Shapefinders provide a direct measure of the geometry as well as the shape of each individual region and complement the indirect methods of estimating the shapes (for example fitting ellipsoids by Furlanetto & Oh 2016). Secondly, our advanced algorithm SURFGEN2, models surfaces through triangulation and the accuracy in measuring the Minkowski functionals and Shapefinders is much better compared to the existing widely used methods, such as the Crofton's formula (Crofton 1868) that is based on cell counting.

Our paper is organized as follows. The simulation of the H I field is briefly described in Section 2. In Section 3, the ionized hydrogen (H II) region is analysed using percolation. The shape of the ionized regions are studied in Section 4. Our conclusions are presented in Section 5.

2 SIMULATING THE NEUTRAL HYDROGEN (H I) DENSITY FIELD

We have generated the neutral hydrogen field using seminumerical simulations. Our seminumerical method involves three main steps: (i) generating the dark matter distribution at the desired redshift, (ii) identifying the location and mass of collapsed dark matter haloes within the simulation volume, (iii) generating the neutral hydrogen map using an excursion set formalism (Furlanetto, Zaldarriaga & Hernquist 2004). The assumption here is that the hydrogen exactly traces the underlying dark matter field and the dark matter haloes host the ionizing sources. We discuss our method in the following paragraphs.

We have used a particle-mesh (PM) *N*-body code to generate the dark matter distribution at desired redshifts. Our simulation volume is a $\sim[215\,\mathrm{Mpc}]^3$ comoving box. We have run our simulation with a 3072^3 grid using 1536^3 dark matter particles. The spatial resolution is 0.07 Mpc that corresponds to a mass resolution of $1.09 \times 10^8\,\mathrm{M}_\odot$.

In the next step, we use the friends-of-friends (FoF) algorithm to identify the location and mass of the collapsed haloes in the dark matter distribution. We have used a fixed linking length, which is 0.2 times the mean interparticle separation and require a halo to have at least 10 dark matter particles that corresponds to a minimum halo mass of $1.09 \times 10^9\,\mathrm{M}_\odot$.

In the final step, we generate the ionization map and the H I distribution using the homogeneous recombination scheme of Choudhury, Haehnelt & Regan (2009). It is assumed that the number of ionizing photons emitted by a source is proportional to the mass of the host halo with the constant of proportionality being quantified through a dimensionless parameter $n_{\rm ion}$. In addition to $n_{\rm ion}$, the simulations have another free parameter $R_{\rm mfp}$, the mean free path of the ionizing photons. The final ionized maps were generated on a grid that is eight times coarser than the *N*-body simulations, i.e. with a spatial resolution of 0.56 Mpc within the simulation volume $\sim[215\,\mathrm{Mpc}]^3$ in comoving scale. Our seminumerical simulations closely follow Majumdar et al. (2014), Mondal et al. (2015), Mondal, Bharadwaj & Majumdar (2016, 2017), and Mondal, Bharadwaj & Datta (2018) to generate the ionization field.

The redshift evolution of the neutral fraction [the fraction of hydrogen mass that is ionized; $x_{\rm H\,I}(z) = \bar{\rho}_{\rm H\,I}(z)/\bar{\rho}_{\rm H}(z)$] during EoR is largely unknown. It is constrained from the CMB anisotropy and polarization measurements (Planck Collaboration XLVI 2016b) and observations of the Lyman-α absorption spectra of the high-redshift quasars (Fan et al. 2003; Becker et al. 2015). These constraints can be satisfied for a wide range of ionization histories. Given the uncertainty of reionization history, the values of reionization model parameters were fixed at $n_{\rm ion} = 23.21$ and $R_{\rm mfp} = 20$ Mpc (Songaila & Cowie 2010) so as to achieve 50 per cent ionization by $z = 8$.

3 PERCOLATION ANALYSIS

We have considered a number of H I density fields with neutral fraction ranging between $x_{\rm H\,I} \in (0.1 - 1.0)$, where the lower limit, $x_{\rm H\,I} = 0.1$, corresponds to the redshift $z \approx 7$ and the upper limit $x_{\rm H\,I} = 1$ corresponds to high redshifts (before reionization was initiated). We study the fully ionized regions within the H I density field having $\rho_{\rm H\,I} = 0$. Side by side, we also consider the complementary region with $\rho_{\rm H\,I} > 0$ and refer to it as the neutral segment. We define the individual regions, in both segments separately, as the connected grid points of same type (ionized or neutral) using the FoF algorithm compatible with the periodic boundary condition (PBC), as explained in Fig. 1.

In percolation analysis, a key role is played by two quantities.

(i) The 'largest cluster statistics' (LCS), defined for the ionized or the neutral segment as (Klypin & Shandarin 1993)

$$\mathrm{LCS} = \frac{\text{volume of the largest neutral or ionized region}}{\text{total volume of all the neutral or ionized regions}}, \quad (1)$$

is the fraction of the volume (ionized or neutral) filled by the largest region.

[1] Percolation has been studied comprehensively in the context of mathematical and condensed matter physics (Essam 1980; Isichenko 1992; Stauffer & Aharony 1994; Saberi 2015).

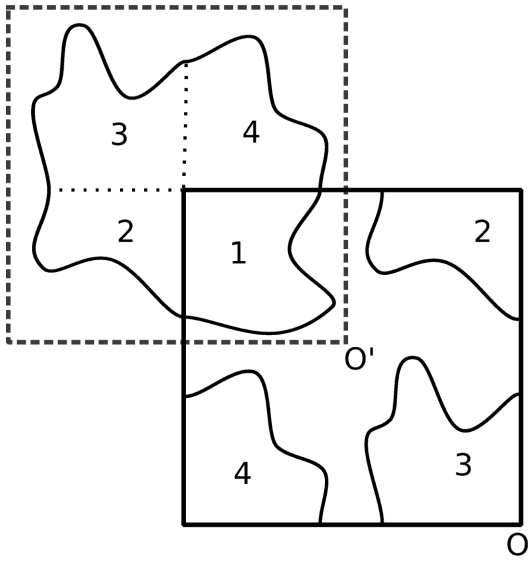

Figure 1. The implementation of PBC is explained using a two-dimensional representation. We define individual regions with connected grid points of same type (neutral or ionized) using FoF algorithm. Due to PBC, the (apparently) disconnected regions appearing the primary box, centred at O, are actually four fragments of one single region. To model the surface of the whole region correctly, while calculating its Minkowski functionals and Shapefinders in Section 4, we restore the whole region to its original shape by simply moving the box to its new origin at O'. This procedure can be easily generalized to 3D.

(ii) The filling factor FF, which is defined for the ionized or the neutral segment as,

$$FF = \frac{\text{total volume of all the neutral or ionized regions}}{\text{volume of the simulation box}}. \quad (2)$$

In the left-hand panel of Fig. 2, we plot the LCS versus the neutral fraction ($x_{\rm H\,I}$) for both the neutral (red) and ionized (blue) segments, while in right-hand panel the plot of LCS versus the filling factor ($FF_{\rm ionized}$) is shown for the ionized segment only.

As reionization progresses, the ionized segment grows in size and so does the largest ionized region. Soon the largest ionized region becomes so large that it stretches from one face of the simulation box to the opposite face. (Note that due to PBC such a region is formally infinite in size.) We refer to this as the 'percolation transition'. During the percolation transition, the LCS increases sharply when plotted against $x_{\rm H\,I}$ or $FF_{\rm ionized}$, as shown in Figs 2(a) and 2(b). Indeed, the percolation transition itself can be identified through this abrupt rise in LCS (Klypin & Shandarin 1993). From both panels of Fig. 2, one finds that the ionized regions percolate for $z \lesssim 9$ (or equivalently $x_{\rm H\,I} \lesssim 0.728$, $FF_{\rm ionized} \gtrsim 0.12$). These critical thresholds at percolation appear to be quite stable for simulations with different resolutions.[2] After percolation, most of the individual ionized regions are rapidly assimilated into the largest ionized region, for example at $x_{\rm H\,I} \approx 0.55$ or $FF_{\rm ionized} \approx 0.3$, almost 90 per cent of the ionized hydrogen resides in the largest ionized region. Therefore, at percolation there is a sharp transition from individual ionized regions to one large connected ionized region. The latter forms by the overlap or merger of the individual ionized regions. This is also evident from Fig. 3 where the largest ionized regions are visualized within the simulation box (of dimension $\sim$215 Mpc^3) at three different values of the neutral fraction corresponding to well before, just before and just after percolation (from left). These results are completely consistent with earlier works, Iliev et al. (2006), Chardin, Aubert & Ocvirk (2012) and Furlanetto & Oh (2016), where different simulation methods were used to generate the H I density fields.

We also find that the neutral segment is percolating (LCS being close to unity) during the entire redshift range under study, namely $7 \lesssim z \lesssim 13$. Therefore, in the range $7 \lesssim z \lesssim 9$ (or equivalently $0.1 \lesssim x_{\rm H\,I} \lesssim 0.728$), both the neutral and ionized parts of the hydrogen field are infinitely extended through their connected regions. As we know, after reionization, the neutral hydrogen remains confined to galaxies and local clusters suggesting that the percolation transition in H I takes place within the range $6 < z < 7$. In the rest of the paper, we focus only on the ionized part, namely H II.

If the ionized bubble size obeys a pure power law distribution,

$$\left(\frac{{\rm d}N}{{\rm d}V'}\right) \propto V^{\tau}, \quad (3)$$

then

$$\mathcal{N}(V) \equiv \int_V^{\infty} \left(\frac{{\rm d}N}{{\rm d}V'}\right) {\rm d}V' = CV^{1+\tau}, \quad (4)$$

is the (cumulative) number of distinct ionized regions, each having minimum volume V. The fraction of ionized volume filled by these $\mathcal{N}(V)$ regions is given by

$$\mathcal{F}(V) \equiv \int_V^{\infty} V' \left(\frac{{\rm d}N}{{\rm d}V'}\right) {\rm d}V' \approx \frac{\left(V_{\rm max}^{2+\tau} - V^{2+\tau}\right)}{\left(V_{\rm max}^{2+\tau} - 1\right)} \quad \text{for } V < V_{\rm max}. \quad (5)$$

In Fig. 4, we plot the bubble size distribution.[3] The solid curves are corresponding to just before percolation (red) and just after percolation (blue) in both the panels while the green dotted and cyan dashed curves are for well before and well after percolation, respectively. $\mathcal{N}(V)$, shown in Fig. 4(a), roughly obeys the power-law distribution, given in equation (4) with $\tau \approx -1.85$, over a large volume range. Clearly, the power-law distribution is more accurate near the percolation transition. These results are overall in accordance with Furlanetto & Oh (2016), but the slope ($\tau \approx -1.85$) in our finding is slightly less compared to their result, $\tau \approx -2$. The power-law distribution ensures that most ionized regions are very small in size without any existence of characteristic bubble size, which has been investigated extensively in literature (Iliev et al. 2006; Friedrich et al. 2011; Lin et al. 2016; Kakiichi et al. 2017). Fig. 4(b) shows behaviour of $\mathcal{F}(V)$, the fraction of ionized volume filled by regions of volume V and higher (defined in equation 5), with the volume V. It is clearly evident that at lower $x_{\rm H\,I}$ beyond percolation, most of the completely ionized volume is enclosed by the largest ionized region. On the other hand, at higher $x_{\rm H\,I}$, smaller regions fill most of the ionized volume. Again, the power-law distribution with $\tau \approx -1.85$ matches quite well with the $\mathcal{F}(V)$ at the onset of percolation.

[2] It would be interesting to study how the percolation transition statistically changes for different models of reionization. Since enormous computational time would be required to carry out this comparison, we leave the exercise for a follow up project.

[3] In Section 3, we calculate the volume of individual ionized regions by counting the grid points inside each region. The number of grid points inside an ionized region roughly reflects its volume. One could have used SURFGEN2, explained in Section 4, to calculate the volume of each individual region more precisely, but that would increase the computation time enormously. Moreover, for extremely small ionized regions, SURFGEN2 would not be very precise because of finite grid effects.

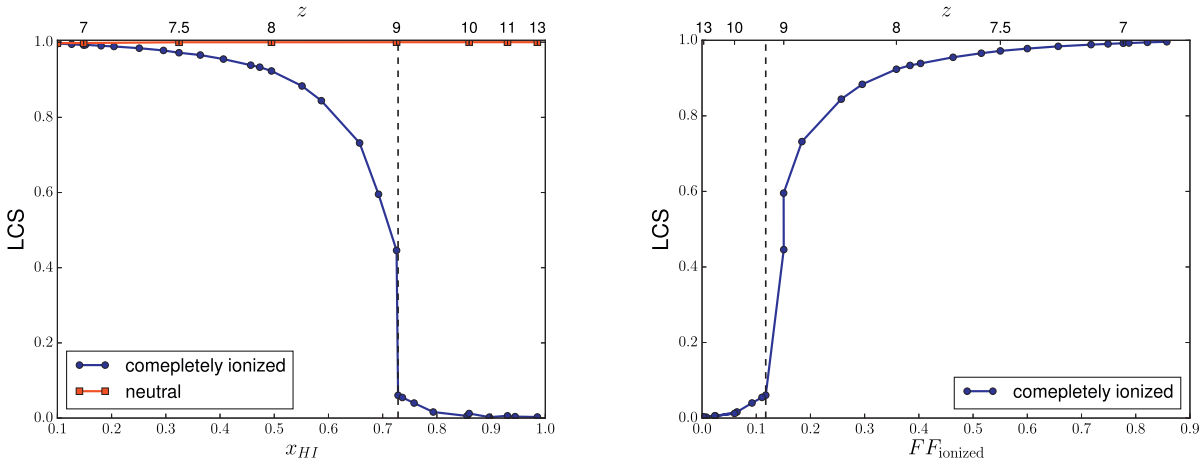

Figure 2. (a): LCS of the ionized regions (with $\rho_{\rm H\,I} = 0$) and the neutral regions (with $\rho_{\rm H\,I} > 0$) are plotted against the neutral fraction $x_{\rm H\,I}$. The corresponding redshift is shown along the top x-axis. The largest neutral region is percolating in the entire range of study, $7 \lesssim z \lesssim 13$. On the other hand, for the ionized regions, the percolation transition takes place at $x_{\rm H\,I} \approx 0.728$, which roughly corresponds to $z \approx 9$, and is shown by the vertical black dashed line. During the percolation transition, the LCS undergoes a sharp rise, as shown in the left-hand panel. (b): the LCS for the ionized regions is plotted against the (ionized) filling factor, $FF_{\rm ionized}$. The largest ionized region starts to percolate at $FF_{\rm ionized} \approx 0.12$ and during the percolation transition LCS increases very steeply as well. We note that the filling factor, $FF_{\rm ionized}$, is essentially the same as the volume weighted ionization fraction.

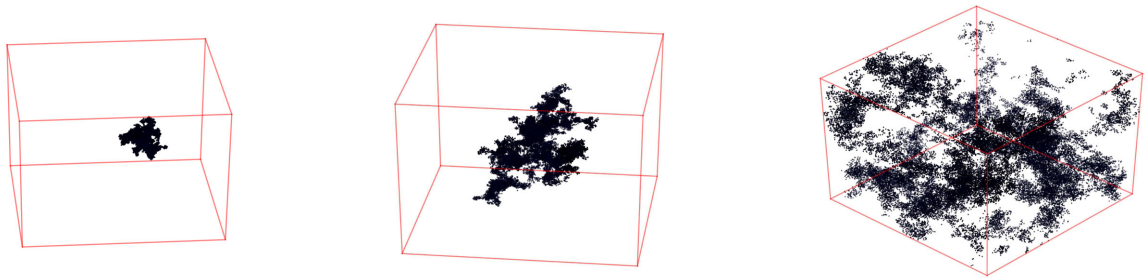

(a) $x_{HI} = 0.793$, well before percolation

(b) $x_{HI} = 0.736$, before percolation

(c) $x_{HI} = 0.726$, just after percolation ($z = 9$)

Figure 3. The largest ionized regions are shown within the simulation box (of dimension $\sim$215 Mpc^3) for three values of the neutral fraction, $x_{\rm H\,I} = 0.793, 0.736, 0.726$ from the left. The corresponding ($FF_{\rm ionized}$, LCS) are (0.064, 0.016), (0.117, 0.061), and (0.151, 0.446), respectively. From the middle panel, it is visually evident that, just before percolation, the largest ionized region becomes like an interconnected filamentary structure with highly non-trivial topology. It becomes formally infinite in size beyond percolation.

4 DETERMINING THE SHAPES OF IONIZED REGIONS USING *SHAPEFINDERS*

In this section, we study the shapes of the ionized regions at different redshifts (various stages of reionization) using Shapefinders, which are derived from Minkowski functionals. The morphology of a closed two-dimensional surface embedded in three dimensions is well described by the four Minkowski functionals (Mecke, Buchert & Wagner 1994).

(i) Volume: V,
(ii) Surface area: S,
(iii) Integrated mean curvature (IMC):

$$C = \frac{1}{2} \oint (\kappa_1 + \kappa_2)\, {\rm d}S, \tag{6}$$

(iv) Integrated Gaussian curvature or Euler characteristic:

$$\chi = \frac{1}{2\pi} \oint (\kappa_1 \kappa_2)\, {\rm d}S. \tag{7}$$

Here, κ_1 and κ_2 are the two principle curvatures at any point on the surface. The fourth Minkowski functional (Euler characteristic) can be written in terms of the genus (G) of the surface as follows:

$$G = 1 - \chi/2 \equiv (\text{number of tunnels}) - (\text{number of isolated surfaces}) + 1. \tag{8}$$

It is well known that χ (equivalently G) is a measure of the topology of the surface.

The 'Shapefinders', introduced in Sahni, Sathyaprakash & Shandarin (1998), are ratios of these Minkowski functionals, namely

(i) Thickness: $T = 3V/S$,
(ii) Breadth: $B = S/C$,
(iii) Length: $L = C/(4\pi)$.

The Shapefinders T, B, L, have dimension of length, and can be interpreted as providing a measure of the three physical dimensions

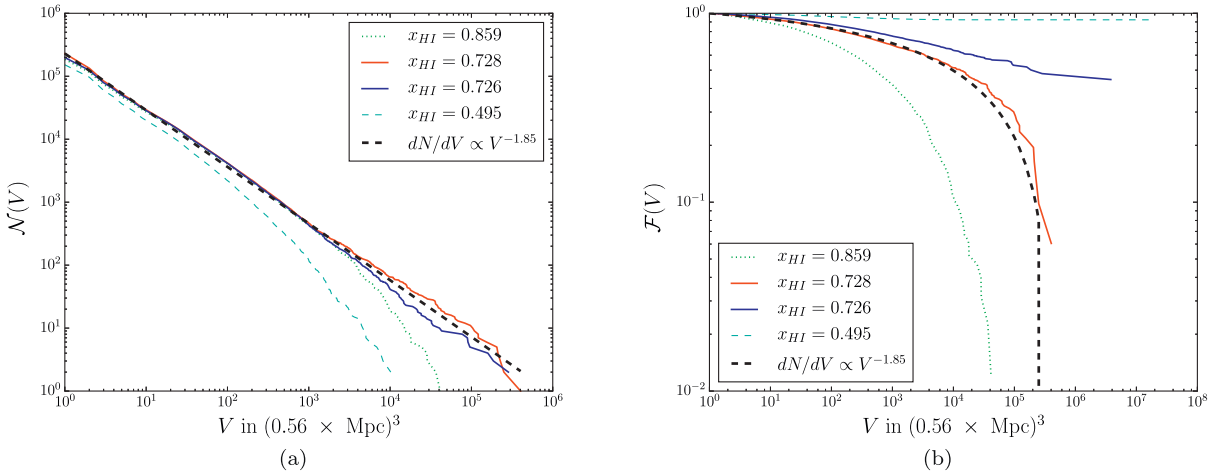

Figure 4. Bubble size distribution: (a): the cumulative number of region $\mathcal{N}(V)$, defined in equation (4), is plotted against ionized region volume for different values of the neutral fraction. The solid curves show the distribution just before (red) and just after (blue) percolation while the green dotted and cyan dashed curves correspond to well before and well after percolation transition, respectively. In this plot, we exclude the largest ionized region after percolation transition. The curves follow the power-law distribution, $\mathcal{N}(V) \propto V^{1+\tau}$ with $\tau \approx -1.85$ (shown by the black dashed line), specially in the vicinity of percolation transition. The distribution with $\tau \approx -1.85$ is slightly less steep than what Furlanetto & Oh (2016) found, $\tau \approx -2$. (b): the fraction of ionized volume filled by the regions with minimum volume V, is plotted for the same set of neutral fractions. We observe that, well after percolation, most of the ionized volume is filled by the largest ionized region. For example, the cyan dashed line shows that at $x_{\rm H\,I} = 0.495$ (corresponds to $z = 8$), the percolating region encloses almost 92 per cent of the ionized volume. On the other hand, well before percolation, most of the ionized volume is distributed in smaller regions. The black dashed line corresponds to the power-law distribution, given in equation (3) with $\tau \approx -1.85$, which matches well with the curve corresponding to just before percolation. Note that here we estimate the volume of each ionized region by counting the grid points inside it. Therefore, the smallest ionized regions have only one grid point inside them that roughly corresponds to volume $V \sim (0.56\,\mathrm{Mpc})^3$.

of an object.[4] The Shapefinders are spherically normalized, i.e. $V = (4\pi/3)T\,B\,L$.

Using the Shapefinders, one can determine the morphology of an object (such as an ionized region), by means of the following dimensionless quantities[5] that characterize its planarity and filamentarity (Sahni, Sathyaprakash & Shandarin 1998)

$$\text{Planarity}: P = \frac{B-T}{B+T}, \quad \text{Filamentarity}: F = \frac{L-B}{L+B}. \tag{11}$$

For a planar object (such as a sheet) $P \gg F$, while the reverse is true for a filament that has $F \gg P$. A ribbon will have $P \sim F \gg 0$ whereas $P \simeq F \simeq 0$ for a sphere. In all cases $0 \leq P, F \leq 1$.

To calculate the Minkowski functionals and the Shapefinders of individual ionized regions, we developed a highly sophisticated code, named SURFGEN2, which models the surfaces of an ionized region through triangulation using *Marching Cube 33* algorithm (Lorensen & Cline 1987; Chernyaev 1995). SURFGEN2 is an advanced version of the SURFGEN algorithm, developed by Sheth et al. (2003). The detailed algorithms are described in Sheth et al. (2003) and Bag et al. (in preparation). The accuracy of SURFGEN2 is excellent and much better than the existing methods of estimating the Minkowski functionals (Schmalzing & Buchert 1997), for example using the Koenderink invariant (Koenderink 1984) or the Crofton's formula (Crofton 1868).

4.1 Shape of the largest ionized region during the percolation transition

Fig. 5 shows how the Minkowski functionals of the largest ionized region evolve during percolation transition, at around $x_{\rm H\,I} \approx 0.728$. During the percolation transition, as the largest ionized region suddenly grows bigger, its Minkowski functionals, namely volume, area, and IMC, increase sharply.[6] But the largest ionized region evolves in such a manner that two of its Shapefinders (ratios of Minkowski functionals), 'thickness' T and 'breadth' B, increase slowly as reionization proceeds. In fact, these two quantities remain almost constant across the percolation transition. In contrast, the third Shapefinder, 'length' L, increases steeply as reionization proceeds (see Fig. 6a) and increases sharply by nearly an order of magnitude at the percolation transition. During the percolation transition, the largest ionized region abruptly grows only in 'length' while the 'cross-section', estimated by $T \times B$, does not change much. One might note that $L \sim 10^3 B$ near the percolation transition. From equation (11), this implies that the largest ionized region is highly filamentary, with 'filamentarity' $F \sim \mathcal{O}(1)$, near percolation. In Fig. 6, the Shapefinders of the largest ionized region are plotted against the region's volume as the latter grows in the vicinity of the percolation transition. Since $V \propto (T \times B \times L)$, L increases

[4] In general, one finds $C > 0$. However in the rare case when a region has $C < 0$, we shall redefine $C \to |C|$ to ensure that B and L are positive. Furthermore, if the natural order $T \leq B \leq L$ is not maintained, we choose the smallest dimension as T and the largest one as L.

[5] One can redefine 'length' by taking the genus (G) of an object into account (Sheth et al. 2003),

$$L_1 = \frac{C}{4\pi(1+|G|)}. \tag{9}$$

This reduces the filamentarity in the following manner while keeping planarity unchanged,

$$F_1 = \frac{L_1 - B}{L_1 + B}. \tag{10}$$

[6] In this paper, all the values of Minkowski functionals and Shapefinders have been quoted in comoving scale.

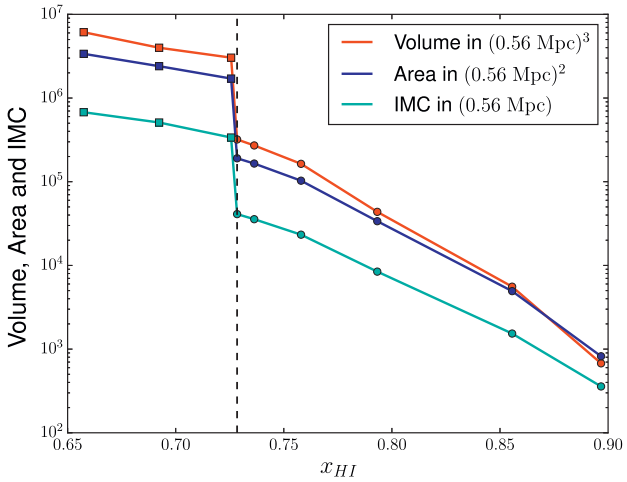

Figure 5. The Minkowski functionals, namely volume, area, and IMC, of the largest ionized region are plotted against neutral fraction ($x_{\mathrm{H\,I}}$) in the vicinity of percolation transition. The percolation transition is shown by the dashed vertical line and the Minkowski functionals of the largest ionized region before and after percolation are shown by filled circles and squares, respectively. Since the largest ionized region grows rapidly during percolation, its volume, area, and IMC increase sharply during percolation transition. All the three Minkowski functionals abruptly rise by almost an order of magnitude. In this paper, all the values of Minkowski functionals and Shapefinders have been quoted in comoving scale.

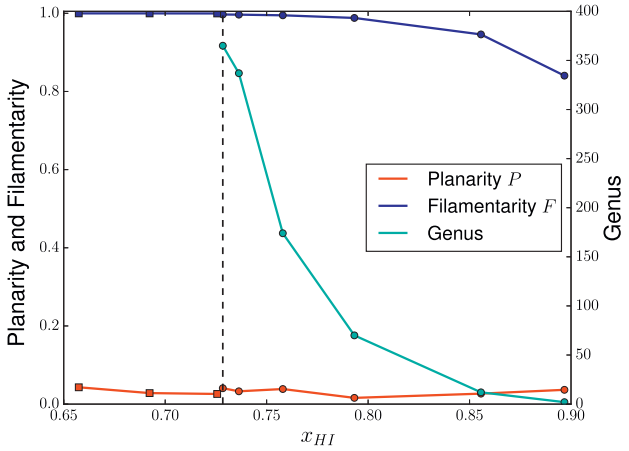

Figure 7. The 'planarity' (P), 'filamentarity' (F), and genus of the largest ionized region are shown as a function of the neutral fraction ($x_{\mathrm{H\,I}}$) in the vicinity of the percolation transition. The filamentarity of the largest ionized region rises to almost unity during percolation but the planarity remains quite small. The genus of the largest ionized region also increases as the region grows. Therefore, the largest ionized region becomes very filamentary and more tunnels pass through the largest ionized region as the latter grows rapidly at the onset of percolation. Note that we do not show the genus value of the largest ionized region after percolation ($x_{\mathrm{H\,I}} < 0.728$), due to uncontrollable errors that arise because of PBC.

almost linearly with volume near percolation where T and B increase much more slowly. The slope of the best-fitting straight line to the $\log L$ versus $\log V$ curve, shown by the dotted cyan line in Fig. 6(b), is of order unity; namely $m_L \equiv \log L/\log V \approx 0.841$. For comparison, $m_L \approx 1/3$ for spherical surfaces, $m_L \approx 1/2$ for sheets and $m_L \approx 1$ for filaments. Hence, we conclude that the largest ionized region possesses a characteristic cross-section ($\sim$7 Mpc^2) that remains almost constant across the percolation transition, while its length grows rapidly near percolation.

As illustrated in Fig. 7, the 'filamentarity' F of the largest ionized region increases reaching almost unity near the percolation transition while the 'planarity' P is quite low and does not vary much. Therefore, the largest ionized region start to become highly

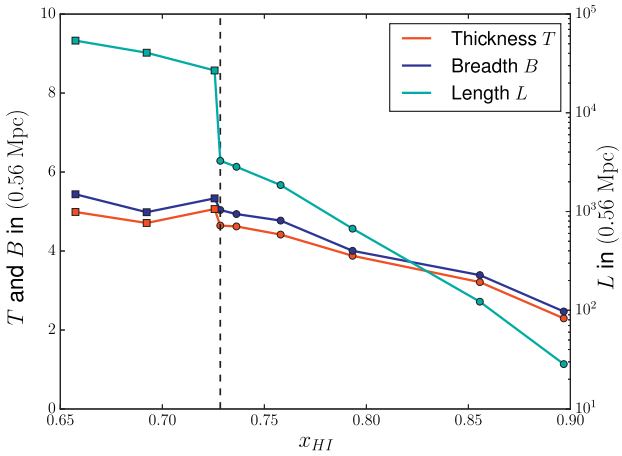

(a)

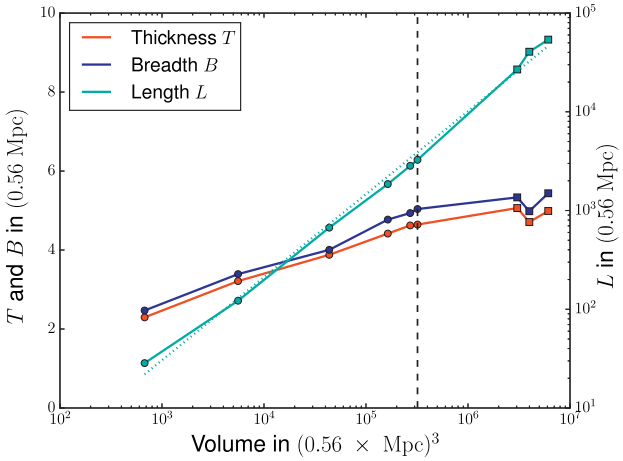

(b)

Figure 6. (a) The volume, area, and the IMC of the largest ionized region grow in such a way that if one computes their ratios, the two Shapefinders – thickness and breadth – do not rise much while the third Shapefinder – length (plotted along right y-axis) – increases rapidly near the percolation transition. Note that, in this paper all the values of Shapefinders are shown in comoving scale. For the largest ionized region, one always obtains $T \approx B \ll L$ in the figures. Near the percolation transition, at $x_{\mathrm{H\,I}} \approx 0.728$, $L \sim 10^3 B$. (b) The Shapefinders of the largest ionized region are plotted against the region's volume as the latter grows during reionization near percolation. The percolation transition is shown by the vertical dashed line in both the panels. The thickness and breadth increase very slowly with volume while length increases almost as power law. The slope of the best-fitting straight line to $\log L$ versus $\log V$ curve, shown by the dotted cyan line, is very close to unity; $m_{\mathrm{L}} = 0.841$. Hence, the length of the largest ionized region increases almost linearly with volume in the vicinity of percolation while the cross-section, estimated by $T \times B$, does not vary much. Therefore, both the panels show that the largest ionized region possesses a characteristic cross-section of $\sim$7 Mpc^2 during its rapid growth near the percolation. Note the enormous difference between T, B on the one hand and L on the other, there is no real intersection of L, B, T, as apparently suggested by the figures.

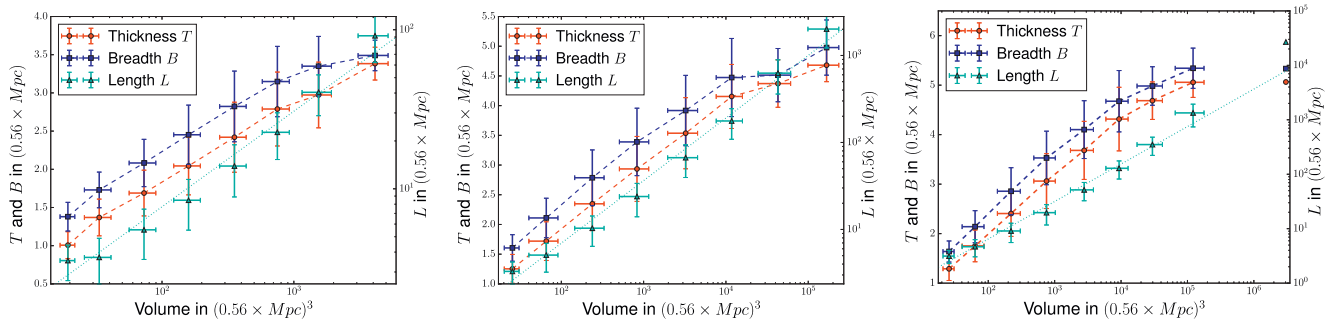

(a) $x_{HI} = 0.856$, well before percolation (b) $x_{HI} = 0.728$, just before percolation (c) $x_{HI} = 0.726$, just after percolation ($z = 9$)

Figure 8. The Shapefinders 'thickness' (T), 'breadth' (B), and 'length' (L) of ionized regions are plotted against their volume in bins, at three different values of neutral fraction. The error bars show standard deviations, which measure the scatter of ionized regions in each bin. The left-hand panel corresponds to $x_{\rm H\,I} = 0.856$ that is well before percolation taking place in the ionized segment. Plots at the onset of percolation, for $x_{\rm H\,I} = 0.728$, are shown in the middle panel. The right-hand panel shows the plots just after percolation, at $x_{\rm H\,I} = 0.726$ (which corresponds to $z = 9$) where we have a large percolating ionized region. In all three figures, the thickness and breadth of ionized regions (plotted in linear scale along the left y-axis) increase much slowly with their volume when compared to the increase in their length with volume (plotted along right y-axis in log scale). We fit straight lines to $\log L$ versus $\log V$ curves, shown by the cyan dotted lines. The slope of the best-fitting straight line, m_L, increases as percolation is approached, for example $m_L \approx 0.60$ in the left-hand panel for $x_{\rm H\,I} = 0.856$ while $m_L \approx 0.72$ at the onset of percolation, as shown in the middle panel. As the calculated Shapefinders of the percolating region in the right-hand panel may suffer from accuracy, we exclude it from fitting. Note that different scales have been used in describing T, B on the one hand and L on the other. A very significant finding our paper is that $T, B \ll L$ for large ionized regions in all three panels. This in turn implies that the large regions are filamentary, from equation (11).

filamentary at the onset of percolation. The genus of the largest ionized region, plotted along the right y-axis in Fig. 7, also increases as reionization proceeds. This implies that as reionization proceeds the largest ionized region acquires an increasingly complex topology with many filamentary branches and subbranches joining it, and several tunnels passing through it.

4.2 Shapes of ionized regions during different stages of reionization

In this subsection, we study the morphology of all ionized regions with Shapefinders at various redshifts. In principle, one can calculate the Shapefinders of all the regions individually by triangulating their surfaces. However, the surfaces of smaller regions, which have only a few grid points inside of them, cannot be accurately modelled by the triangulation scheme. Consequently, their value of Minkowski functionals and Shapefinders suffer in accuracy due to low resolution. Moreover, since the number of ionized regions is very large near the percolation transition, calculating Shapefinders for all of them takes enormous computational time. Therefore, in this study we consider only sufficiently large ionized regions, with at least 50 grid points inside each one, for the purpose of efficient triangulation.

The Shapefinders, 'thickness' (T), 'breadth' (B), and 'length' (L), of ionized regions are plotted against their volume in Fig. 8 for three different values of neutral fraction $x_{\rm H\,I}$. The regions are binned in volume (equispaced bin width in log scale) and the error bars show standard deviations, which measure the scatter of ionized regions in each bin. The values of the neutral fraction $x_{\rm H\,I}$ in the panels of Fig. 8 correspond to, commencing from the left: (a) well before percolation ($x_{\rm H\,I} = 0.856$), (b) just before percolation ($x_{\rm H\,I} = 0.728$), and (c) just after percolation ($x_{\rm H\,I} = 0.726$). In all cases, one notices that the thickness (T) and the breadth (B) (plotted in linear scale along the left y-axis) of the large ionized regions increase somewhat more slowly with volume when compared to the increase in length (L) with their volume (plotted along the right y-axis in log scale). This feature is more pronounced at the onset of percolation (middle panel). Since many large ionized regions appear as the percolation transition is approached, the cross-section of larger ionized regions, measured by ($T \times B$), are more alike near percolation. We join the values of T and B in bins with dashed lines for visual guidance and fit straight lines to $\log L$ versuslog V curves. The slope of the best-fitting straight line (shown by the dotted line), m_L, increases as the neutral fraction approaches the critical value at percolation $x_{\rm H\,I}^C \approx 0.728$. For example, $m_L \approx 0.60$ in the left-hand panel for $x_{\rm H\,I} = 0.856$ while $m_L \approx 0.72$ at the onset of percolation for $x_{\rm H\,I} = 0.728$, as shown in the Figs 8(a) and 8(b), respectively. Also, the fit itself gets better near percolation; therefore large ionized regions show a power-law dependence of length on their volume, which is more valid in the vicinity of percolation transition, just like the growth of the largest ionized region. After percolation, there exists a large percolating region, as shown in Fig. 8(c). Since its Shapefinders may not be calculated accurately, we exclude it from fitting or joining. Well beyond percolation, the largest ionized region continues to grow and the rest of the ionized regions become smaller in number as well as in size. These scenarios are less important and have therefore been excluded from our Shapefinder analysis.

The planarity, filamentarity, and genus of ionized regions are shown in Fig. 9. The same set of values of neutral fraction is used as in Fig. 8. The filamentarity and genus are joined by dashed lines for visual guidance while the planarity is fitted with a (dotted) straight line. It is interesting to note that the filamentarity of ionized regions increases with volume while the planarity slowly decreases with increasing volume. This explicitly demonstrate that large ionized regions are very filamentary around the percolation threshold.

The genus, plotted along right y-axis in Fig. 9, also increases with volume, i.e. more tunnels pass through larger ionized regions. This suggests that large filamentary ionized regions are multiply connected with non-trivial topology. The characteristic cross-section of these large regions is well described by $T \times B \sim 7\,{\rm Mpc}^2$ near

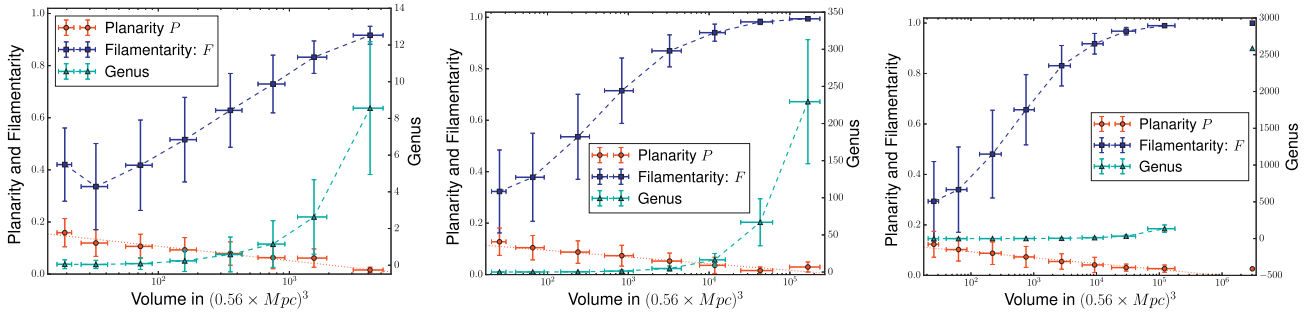

(a) $x_{HI} = 0.856$, well before percolation (b) $x_{HI} = 0.728$, just before percolation (c) $x_{HI} = 0.726$, just after percolation ($z = 9$)

Figure 9. To understand the shapes of the ionized regions, their 'planarity' (P) and 'filamentarity' (F) are plotted in volume bins at three different values of neutral fraction. The error bars show standard deviations, which measure the scatter of ionized regions in each bin. The left-hand panel corresponds to $x_{\rm H\,I} = 0.856$ that is well before percolation taking place in the ionized segment. Plots at the onset of percolation, for $x_{\rm H\,I} = 0.728$, are shown in the middle panel. The right-hand panel shows the plots just after percolation, at $x_{\rm H\,I} = 0.726$ (which corresponds to $z = 9$) where we have a large percolating ionized region. In all the three figures, the filamentarity of ionized regions increases with their volume. In contrast, the planarity of ionized regions does not change rapidly, in fact it decreases very slowly with increasing volume. Hence, the large ionized regions become very much filamentary. On the other hand, by extrapolating the curves to the lower volume, we observe that filamentarity and planarity (as well as genus) would be quite small which suggests that the most of the smaller regions have somewhat spherical morphology. But surprisingly, in the left-hand panel (at very early stage of reionization), the filamentarity of extremely small ionized regions actually increases with decreasing volume. This indicates that at very early stages of reionization, most of the first small ionized bubbles are not exactly spherical but have trivial topology.

percolation. One concludes that large ionized regions grow via the merging of relatively smaller ionized regions that were themselves large enough to be quite filamentary and to possess similar cross-sections. On the other hand, by extrapolating the curves towards lower volume, one finds that both filamentarity and planarity (as well as genus) of smaller regions can be quite low. Hence, smaller regions are quite spherical with trivial topology.

In Figs 8 and 9, the standard deviations in each volume bin are shown by the respective error bars. It is evident from these figures that the error bars on the first two Shapefinders – thickness (T) and breadth (B) – as well as on the planarity (P) and filamentarity (F) shrink as we move to higher volume bins. As we know, the large regions are formed by many interconnected filamentary branches and subbranches (substructures) joining together. These substructures are large enough to possess similar values of T, as well as B. The Shapefinders, T and B of large ionized regions are somewhat averaged thickness and breadth of all these substructures. Therefore, T, as well as B, of larger ionized regions are more alike because the number of substructures is higher. In comparison, the smaller ionized regions have lesser number of substructures resulting in slightly more diverse T and B. Hence, despite having fewer ionized regions in higher volume bin, the standard deviations (shown by the error bars) in T and B, as well as in P, are smaller in higher volume bins. This leads to the characteristic cross-section in the large regions. On the other hand, the filamentarity (F) increases with region volume and F of large regions are already very close to unity. Therefore, the scatter in F is much less in higher volume bins. Smaller regions are lesser filamentary in general and have comparatively diverse morphology. Note that the error bars on volume, length (L), and genus do not shrink in higher volume bins.

One intriguing fact to note is that in the early stages of reionization, the filamentarity of very small ionized regions actually increases slightly as we move to smaller ionized regions, see Fig. 9(a). This characteristic is quite robust and can be found in all H I density fields at early stages of reionization. Another interesting fact is that planarity of ionized regions slightly increases with decreasing volume at all stages of reionization. These features indicate that early ionized bubbles are not exactly spherical but mostly have trivial topology. Unfortunately, due to coarse resolution, we cannot precisely calculate Shapefinders for extremely small ionized bubbles.

5 CONCLUSION AND DISCUSSIONS

Minkowski functionals and Shapefinders are powerful means of studying the geometry and topology of large-scale structures. We employ them in conjunction with percolation analysis, to study the morphology of the H I density field, simulated using the 'inside-out' model of reionization. In this paper, we use the LCS to study the percolation transition. Concerning the neutral hydrogen, we find LCS $\approx$1 through the entire redshift range that we have considered, $7 \lesssim z \lesssim 13$. This informs us that there is a single large neutral region that persists as reionization proceeds. This region percolates through the entire simulation box spanning from one face of the simulation volume to the other and formally has infinite volume.

On the other hand, concerning the ionized regions, we find that the LCS has a small value during the early stages of reionization. As reionization proceeds, we find the onset of a transition, the percolation transition, beyond which the LCS increases sharply to attain a value $\approx$1 that is maintained through the subsequent stages of reionization. The percolation transition in the ionized regions takes place at the critical neutral fraction $x^C_{\rm H\,I} \approx 0.728$, when almost 12 per cent simulation volume is filled by the ionized hydrogen (H II), i.e. the critical filling factor $FF^C_{\rm ionized} \approx 0.12$. These results agree well with the previous findings of Iliev et al. (2006), Chardin et al. (2012) and Furlanetto & Oh (2016). After percolation most of the ionized volume is rapidly filled by an enormous (formally infinite) region. In the vicinity of percolation, the ionized regions follow a power-law distribution for a large interval in volume.; $dn/dV \propto V^{\tau}$ where $\tau \approx -1.85$. This is consistent with the results of Furlanetto & Oh (2016), who find $\tau \approx -2$ for the H I fields simulated using the 21CMFAST code.

The study of Shapefinders in the vicinity of percolation reveals that, as the largest ionized region grows with reionization, its Minkowski functionals increase but their ratios, the first two Shapefinders – thickness (T) and breadth (B) – do not increase much. However, the third Shapefinder – length (L) – increases

almost linearly with volume, $L \propto V^{0.841}$. Consequently, $L \gg B \simeq T$ for the largest ionized region. The product of thickness and breadth, $T \times B$, provides a measure of 'cross-section' of a filament-like region. We find that the largest ionized region possesses a characteristic cross-section of $\sim 7\,\mathrm{Mpc}^2$ that does not vary much near the percolation transition, while the length of this region increases abruptly. This makes the largest ionized region become very filamentary at the onset of percolation. As the largest ionized region grows, its genus increases, i.e. more tunnels pass through it. Hence, the shape and the topology of the largest ionized region becomes more complex with time.

We also study the Shapefinders of all ionized regions at various stages of reionization. We find that, at a fixed redshift, larger ionized regions are in general more filamentary and their cross-sections increase more slowly with their volumes compared to the increase in their lengths. As more large ionized regions start to appear near the percolation transition, this feature becomes more pronounced. In addition, the genus value is higher for larger ionized regions that is suggestive of their being multiconnected with complex topology. This could be because larger ionized regions grow via the merging of many filament-like smaller ones.

As the first in a series of papers meant to explore the shape statistics of the reionization field, this work investigates the topology and morphology of ionized bubbles as they evolve during reionization. The morphology, studied using percolation, Minkowski functionals and Shapefinders, is richer in information than more conventional probes of reionization, e.g. the two-point correlation function. In a companion paper (Bag et al., in preparation), we shall study the morphology of H I overdense and underdense excursion sets using similar tools. We also plan to include other models of reionization in our analysis and compare the topology and morphology of H I density fields simulated using these models. We also wish to extend our analysis to understand whether the data from upcoming low-frequency interferometers, such as SKA, HERA, can be used for calculating the Shapefinders. This would involve computing the Shapefinders in the presence of instrument noise and astrophysical foregrounds.

ACKNOWLEDGEMENTS

The authors would like to acknowledge useful discussions with Tirthankar Roy Choudhury, Santanu Das, Aseem Paranjape, and Ajay Vibhute. SB thanks the Council of Scientific and Industrial Research (CSIR), India, for financial support as senior research fellow. The H I simulations, used in this work, were done at the computational facilities at the Centre for Theoretical Studies, IIT Kharagpur, India. The numerical computations, related to percolation and shape analyses, were carried out using high performance computation (HPC) facilities at IUCAA, Pune, India.

REFERENCES

Ali Z. S. et al., 2015, ApJ, 809, 61
Barkana R., Loeb A., 2001, Phys. Rep., 349, 125
Becker R. H. et al., 2001, AJ, 122, 2850
Becker G. D., Bolton J. S., Madau P., Pettini M., Ryan-Weber E. V., Venemans B. P., 2015, MNRAS, 447, 3402
Bowman J. D. et al., 2013, Publ. Astron. Soc. Aust., 30, e031
Chardin J., Aubert D., Ocvirk P., 2012, A&A, 548, A9
Chernyaev E. V., 1995, Technical Report CERN-CN-95-17
Choudhury T. R., Haehnelt M. G., Regan J., 2009, MNRAS, 394, 960
Crofton M. W., 1868, Phil. Trans. R. Soc. Lond., 158, 181
DeBoer D. R. et al., 2017, PASP, 129, 045001
Dillon J. S. et al., 2014, Phys. Rev. D, 89, 023002
Essam J. W., 1980, Rep. Prog. Phys., 43, 833
Fan X. et al., 2003, AJ, 125, 1649
Friedrich M. M., Mellema G., Alvarez M. A., Shapiro P. R., Iliev I. T., 2011, MNRAS, 413, 1353
Furlanetto S. R., Oh S. P., 2016, MNRAS, 457, 1813
Furlanetto S. R., Zaldarriaga M., Hernquist L., 2004, ApJ, 613, 16
Furlanetto S. R. et al., 2009, Astro2010: The Astronomy and Astrophysics Decadal Surveyc, Science White Papers, p. 82 (arXiv:0902.3259) [astro-ph.CO]
Goto T., Utsumi Y., Hattori T., Miyazaki S., Yamauchi C., 2011, MNRAS, 415, L1
Iliev I. T., Mellema G., Pen U.-L., Merz H., Shapiro P. R., Alvarez M. A., 2006, MNRAS, 369, 1625
Iliev I. T., Mellema G., Ahn K., Shapiro P. R., Mao Y., Pen U.-L., 2014, MNRAS, 439, 725
Isichenko M. B., 1992, Rev. Mod. Phys., 64, 961
Jacobs D. C. et al., 2015, ApJ, 801, 51
Kakiichi K. et al., 2017, MNRAS, 471, 1936
Kapahtia A., Chingangbam P., Appleby S., Park C., 2017, preprint (arXiv:1712.09195)
Klypin A., Shandarin S. F., 1993, ApJ, 413, 48
Koenderink J. J., 1984, Biol. Cybern., 50, 363
Komatsu E. et al., 2011, ApJS, 192, 18
Koopmans L. et al., 2015, Advancing Astrophysics with the Square Kilometre Array (AASKA14), 1
Lin Y., Oh S. P., Furlanetto S. R., Sutter P. M., 2016, MNRAS, 461, 3361
Lorensen W. E., Cline H. E., 1987, Comput. Graph., 21, 163
Majumdar S., Mellema G., Datta K. K., Jensen H., Choudhury T. R., Bharadwaj S., Friedrich M. M., 2014, MNRAS, 443, 2843
Mecke K. R., Buchert T., Wagner H., 1994, A&A, 288, 697
Mellema G. et al., 2013, Exp. Astron., 36, 235
Mitra S., Choudhury T. R., Ferrara A., 2015, MNRAS, 454, L76
Mondal R., Bharadwaj S., Majumdar S., Bera A., Acharyya A., 2015, MNRAS, 449, L41
Mondal R., Bharadwaj S., Majumdar S., 2016, MNRAS, 456, 1936
Mondal R., Bharadwaj S., Majumdar S., 2017, MNRAS, 464, 2992
Mondal R., Bharadwaj S., Datta K. K., 2018, MNRAS, 474, 1390
Ota K. et al., 2017, ApJ, 844, 85
Ouchi M. et al., 2010, ApJ, 723, 869
Paciga G. et al., 2013, MNRAS, 433, 639
Parsons A. R. et al., 2014, ApJ, 788, 106
Planck Collaboration XVI, 2014, A&A, 571, A16
Planck Collaboration XIII, 2016a, A&A, 594, A13
Planck Collaboration XLVI, 2016b, A&A, 596, A107
Robertson B. E., Ellis R. S., Furlanetto S. R., Dunlop J. S., 2015, ApJ, 802, L19
Saberi A. A., 2015, Phys. Rep., 578, 1
Sahni V., Sathyaprakash B. S., Shandarin S. F., 1998, ApJ, 495, L5
Schmalzing J., Buchert T., 1997, ApJ, 482, L1
Shandarin S. F., 1983, Sov. Astron. Lett., 9, 1046
Shandarin S. F., Sheth J. V., Sahni V., 2004, MNRAS, 353, 162,
Sheth J. V., Sahni V., Shandarin S. F., Sathyaprakash B. S., 2003, MNRAS, 343, 22,
Sheth J. V., 2004, MNRAS, 354, 332
Sheth J. V., Sahni V., 2005, preprint (astro-ph/0502105)
Songaila A., Cowie L. L., 2010, ApJ, 721, 1448
Stauffer D., Aharony A., 1994, Introduction to Percolation Theory. CRC Press, New York
Trenti M., Stiavelli M., Bouwens R. J., Oesch P., Shull J. M., Illingworth G. D., Bradley L. D., Carollo C. M., 2010, ApJ, 714, L202
van Haarlem M. P. et al., 2013, A&A, 556, A2
Yatawatta S. et al., 2013, A&A, 550, A136
Yoshiura S., Shimabukuro H., Takahashi K., Matsubara T., 2017, MNRAS, 465, 394
Zheng Z.-Y. et al., 2017, ApJ, 842, L22

This paper has been typeset from a TEX/LATEX file prepared by the author.